Characterization of the neurogenic niche in the aging dentate gyrus using iterative immunofluorescence imaging

John Darby Cole[1], Jacobo Sarabia del Castillo[2], Gabriele Gut[2], Daniel Gonzalez-Bohorquez[1], Lucas Pelkmans[2], Sebastian Jessberger[1#]

[1]Laboratory of Neural Plasticity, Faculties of Medicine and Science, Brain Research Institute, University of Zurich, 8057 Zurich, Switzerland. [2]Department of Molecular Life Sciences, University of Zurich, 8057 Zurich, Switzerland [#]Correspondence should be addressed to S.J. (jessberger@hifo.uzh.ch)

Abstract

Advancing age causes reduced hippocampal neurogenesis, associated with age-related cognitive decline. The spatial relationship of age-induced alterations in neural stem cells (NSCs) and surrounding cells within the hippocampal niche remains poorly understood due to limitations of antibody-based cellular phenotyping. We established iterative indirect immunofluorescence imaging (4i) in tissue sections, allowing for simultaneous detection of 18 proteins to characterize NSCs and surrounding cells in young and aged mice. We show that reorganization of the DG niche already occurs in middle-aged mice, paralleling the decline in neurogenesis. Tissue 4i-based analysis of the DG identifies changes in cell-type contributions to the blood brain barrier and microenvironments surrounding NSCs to play a pivotal role to preserve neurogenic permissiveness. The data provided represent a resource to characterize the principles causing alterations of stem cell-associated plasticity within the aging DG and provide a blueprint to analyze somatic stem cell niches across lifespan in complex tissues.

Introduction

Somatic stem cells divide throughout life to generate progeny that is required for tissue homeostasis and repair (Fuchs and Segre, 2000). With advancing age, there is a decline in stem cell numbers, output, and function, which has been associated to altered organ integrity and reduced tissue repair in aging mammals (Ermolaeva et al., 2018). In addition to age-dependent, cell-intrinsic alterations causing reduced functionality of somatic stem cells, there is ample evidence that changes in the surrounding stem cell niche contribute to age-related stem cell phenotypes (Morrison and Spradling, 2008; Dulken et al., 2019; Navarro Negredo et al., 2020). However, the exact spatial relationships between altered niche cells and somatic stem cells remain incompletely understood, likely due to the fact that conventional immunohistochemical approaches only allow for the simultaneous detection of few proteins. Further, conventional RNA sequencing approaches or proteome analyses do not allow for the recovery of spatial information within complex tissues. Thus, recent work aimed to overcome these limitations, for example by the development of spatial transcriptomics, multiplexed protein detection, and mass-spectrometry based approaches allowing for the detection of dozens of proteins with cellular resolution (Giesen et al., 2014; Stahl et al., 2016; Schapiro et al., 2017; Lin et al., 2018; Schulz et al., 2018; Burgess, 2019; Moncada et al., 2020). Based on these technological innovations major advances have been achieved characterizing the cellular organization and complexity of mouse and human tissues in health and disease (Decalf et al., 2019; Wagner et al., 2019). However, these approaches largely miss three-dimensional information

in tissues and require highly specialized equipment and/or customized or conjugated antibodies, reducing their availability. Modifying recently developed 4i (iterative, indirect, immunofluorescence imaging) technology, established in cultured, monolayer cells and allowing for the detection of dozens of individual proteins within single cells (Gut et al., 2018), we here developed a robust protocol using conventional antibodies in histological tissue sections to characterize the cellular architecture and protein expression in complex mouse and human tissues. We applied tissue 4i to characterize the aging dentate gyrus (DG) niche of the mouse hippocampus, one of the brain areas where neural stem cells (NSCs) generate new neurons throughout life (Gage, 2019). Advancing age has been associated with strongly reduced NSC activity and diminished neuronal output, which is due to cell-intrinsic, niche-dependent, and humoral mechanisms (Villeda et al., 2011; Moore et al., 2015; Boldrini et al., 2018; Kalamakis et al., 2019; Moreno-Jimenez et al., 2019; Tobin et al., 2019; Denoth-Lippuner and Jessberger, 2021). Using tissue 4i we show that the cellular reorganization of the DG niche occurs relatively early in life and identify substantial alterations in contact sites between NSCs and the vasculature, and niche-associated changes that are paralleled with a decline in neurogenesis. The data presented here characterize age-related changes in the DG niche and provide a blueprint for the analyses of a substantial number of proteins in single cells and their surrounding niche within complex tissues.

Results

Tissue 4i in complex mouse and human tissues

To achieve multiple rounds of tissue 4i sections needed to be adequately mounted to minimize loss of samples through detachment without affecting antigenicity. Coating the glass-bottomed well-plates with poly-d-lysine (PDL) was effective to preserve tissue adhesion across multiple cycles of tissue 4i in sections of 3-month-old adult mouse brain (Figure 1A), human embryonic stem cell (hESC)-derived regionalized forebrain organoids (Figure 1B), and embryonic day 14.5 (E14.5) mouse brain (Figure 1C). Thus, using this approach, sequential rounds of antibody stainings in mouse and human tissues becomes achievable (Figure 1A-C, for details of used antibodies refer to legend of Figure 1). Notably, tissue 4i allows for 3-dimensional reconstruction of tissue volumes, facilitating detailed spatial analyses throughout tissue sections (Figure 1D), showcased using antibodies against IBA1-labeled microglia, Nestin- and GFAP-labeled NSC processes, DCX-expressing immature neurons, LaminB1-expressing cells, and CollagenIV-labeled vasculature (Figure 1D). To assess potential effects of cyclic staining and repeated elutions on sample antigenicity, adult brain sections were stained with a representative set of marker proteins (HOPX, hippocampal NSCs; IBA1, microglia; SOX2, NSCs and astrocytes), imaged, and subsequently subjected to six rounds of elution prior to restaining. Measured fluorescence intensities between the stainings before and after rounds of elution were strongly correlated (Figure 1E), indicating that antigenicity is

preserved across repeated cycles of iterative immunostainings in tissue sections.

Cellular alterations in the DG niche with age

After establishing a robust protocol for iterative immunostainings in complex tissues, we used tissue 4i to analyze age-associated cellular and molecular alterations in the dentate gyrus (DG) of the hippocampal formation. NSCs generate new neurons throughout life in the DG. However, hippocampal neurogenesis is significantly decreasing during adulthood (Ben Abdallah et al., 2010; Denoth-Lippuner and Jessberger, 2021). To test for tissue 4i's ability to identify age-related changes within the DG, a panel of antibodies were applied iteratively on the exact same sections to visualize a number of diverse cell types in 2-, 6- and 12-month-old brain sections: "Stem cells" were visualized using HOPX, Nestin, GFAP, SOX2, ID4, MT3, LaminB1; "Proliferation" was assessed using pH3, KI67, "Neurons" were labeled with DCX, PV, ARC, LaminB1, "Glial cells" were stained for NG2, OLIG2, IBA1, S100β, "Vasculature" was analyzed with CD13 and Collagen IV (Figure 2A-D and Figure 2 Supplement 1-4) (Ben Abdallah et al., 2010; Denoth-Lippuner and Jessberger, 2021). Neurogenic cells were classified in radial glia-like stem cells (R, also referred to as type 1 cells), based on Nestin expression and the extension of a radial process (Denoth-Lippuner and Jessberger, 2021). Further, R cells were phenotyped based on combinatorial expression of HOPX and glial fibrillary acidic protein (GFAP) (Denoth-Lippuner and Jessberger, 2021). As both HOPX and GFAP are also expressed in astrocytes, only cells that were negative for the astrocytic calcium-binding

protein S100β, a marker for mature astrocytes, were considered to be R cells. Proliferating non-radial (NR cells) were identified in the subgranular zone (SGZ) by the expression of KI67 and absence of a GFAP-labeled radial process. Immature neurons were classified based on doublecortin (DCX) expression.

Using the whole panel of antibodies, distinct cell types were quantified in the subgranular zone SGZ and normalized to the volume of the DG granule cell layer (GCL) (Figure 3A-C). As expected, the quantity of R cells was significantly reduced in aged animals (Figure 3A-B) (Denoth-Lippuner and Jessberger, 2021). While the total number of proliferating KI67-positive cells decreased with age, KI67-positive R cells did not change. Additionally, the number of immature neurons, positive for DCX was strongly reduced at 12 months of age (Figure 3A-B).

In the neurogenic niche, R cells interact with and are regulated by several different cell types that are present within their DG niche (Song et al., 2016; Mosher and Schaffer, 2018). To assess potential changes in the cytoarchitecture of the neurogenic niche, microglia, astrocytes, and oligodendrocytes were counted and normalized to the total tissue volume as well as the sub-regions of the DG, the molecular layer (ML), GCL, and hilus. There were no significant differences in IBA1-labeled microglia, or oligodendrocyte precursor cells (OPCs, expressing OLIG2 and NG2) in the DG or within the analyzed DG sub-regions (Figure 2A-B and Figure 3C). However, in aged animals, the numbers of astrocytes, expressing S100β, in the whole DG were reduced (Figure 3A, C).

We next used tissue 4i to analyze expression levels of selected proteins and their potential correlations. We focused on HOPX and MT3, which have been identified to be present in R cells and may be related with R cell quiescence (Shin et al., 2015; Berg et al., 2019; Bottes et al., 2021). Supporting previous data suggesting that advancing age is associated with increased R cell quiescence (Kalamakis et al., 2019; Harris et al., 2021), we identified in 12-month-old animals increased fluorescent intensities of HOPX and MT3 (Figure 4A).

To further validate the tissue 4i approach, we analyzed age-related expression of LaminB1 (LB1), one of the four intermediate filaments that make up the nuclear lamina, and where reductions with aging and the premature aging phenotype of progeria have been previously described (Burke and Stewart, 2013). Confirming previous reports, we found reduced levels of LB1 between 2- and 12-month-old animals in R cells and DCX-labeled, immature neurons (Bedrosian et al., 2021; Bin Imtiaz et al., 2021). tissue 4i now allows for analyzing expression levels in other cell types within exactly the same sections: microglia, astrocytes, and Parvalbumin (PV)-labeled interneurons in the niche showed no significant changes with age in their LB1 expression levels (Figure 4B).

Decline of vascular network and alterations of BBB composition with age

In the DG, both R and NR cells have close relationships with surrounding blood vessels that are the source of regulatory trophic factors, originating from vascular endothelial cells, and connect the neurogenic niche to the circulating blood system. Across species, the hippocampus shows a strong age-related

decline in vascularization (Katsimpardi et al., 2014; Boldrini et al., 2018). tissue 4i-based analysis confirmed that vascular density decreases with age, with reductions already visible by 6 months of age (Figure 5A-B). In addition to declining vascular networks, age has been associated with an increase in leakiness of the blood brain barrier (BBB), potentially permitting molecules into the brain leading increased inflammation and neurotoxicity (Bell et al., 2010). BBB integrity was estimated by measuring the percent of vasculature covered by other cell types based on signal co-localization. While there was no significant change in the total percentage of vasculature coverage, differences were observed in the contributions of different cell types (Figure 5C-D). Pericytes, expressing CD13 and representing one of the primary cell-type that make up the BBB (Bell et al., 2010), were significantly reduced at 6 months with area covered remaining stable at 12 months. Interestingly, there appeared to be a compensatory increase in coverage by astrocytes (Figure 5C-D). Additionally, there was a strong trend for an increase in microglia-blood vessel contact at 6 months that reached significance in 12-month-old mice compared to young adult mice (Figure 5C-D). The contribution of R cells (expressing Nestin) to vasculature coverage significantly decreased with age likely due to the decrease in population, while OPC (labeled with NG2) contact sites with the vasculature remained consistent at each age point (Figure 5C-D).

Microniche-based analysis identifies novel characteristics of the aged DG

To utilize the multidimensionality of the dataset acquired with tissue 4i, the GCL and bordering areas of the hilus and molecular layer were randomly

subdivided and volumes of cell types were measured within those "microniches" (Figure 6A). *Post hoc* analysis showed significant differences (in terms of percent of marker expression per randomized microniche volume) in a variety of measured cell types within microniches (Figure 6B). For example, vascular and pericyte densities were similarly decreased at 6 and 12 months compared to 2-month-old mice. While the stem cell marker Nestin was significantly reduced by 6 months, GFAP, which is also present in classical astrocytes, remained stable between each age point (Figure 6B). Additionally, SOX2 was reduced at 6 months, and decreased further in 12-month-old animals. For glial cells, IBA1-expressing microglia sequentially increased with age while OPCs showed a temporary increase at 6 months with a trending decrease at 12 months (Figure 6B). Thus, tissue 4i allows for the identification of cell type specific alterations with age.

For dimensional reduction, principal component analysis (PCA) was used to cluster the sample regions based on their cellular contents. The majority of regions from 2-month-old animals formed a cluster that was distinct from 6 and 12-month-old animals, which primarily clustered together (Figure 6C). As the spots largely segregated into two groups, k-means clustering was performed expecting two populations; one "young-like" and one "old-like" identified based on neurogenic cell content. In the 2-month-old animals, 64.5% of spots were grouped as young while 35.5% were labeled as old (Figure 6D). Comparing the contents of the two classes of spots, "young" spots showed higher volumes of Nestin, SOX2, KI67, DCX, CollagenIV, PV, IBA1, and NG2 (Figure 6E). As such, the development of an "aged" phenotype occurred for select niches already at 2 months of age and became

already very pronounced in 6-moth-old mice. To explore the potential of protective microenvironments within the DG, spots were split by Nestin radial process content. Spots containing a population of Nestin-labeled R cells were identified as falling within the top three quartiles of spots identified in young mice (0.4% volumetric coverage) (Figure S6a). At 2 months, there were no differences in the volumes of CollagenIV vasculature or IBA1-expressing microglia between high and low nestin populated spots (Figure 6F). However, in both the 6- and 12-month- old groups, both CollagenIV and IBA1 were robustly elevated in the “high” Nestin spots (Figure 6F). In contrast, spots containing Ki67-positive proliferating cells, CollagenIV and IBA1 volumes were comparable to Ki67-negative spots from middle-aged and aged animals (Figure 6B-D). Thus, tissue 4i was used to identify preferential occupancy of blood vessels and IBA1-labeled cells in Nestin-containing microniches, indicating a potential role for the vasculature and microglial cells in the maintenance of quiescent stem cells.

Age-dependent dynamics of stem cell contact sites in the DG niche

Taking advantage of the ability to analyze three-dimensional cellular interactions using tissue 4i, we next characterized the contacts of radial processes extending from R cells (Seri et al., 2001; Kronenberg et al., 2003). While little is still known about the function of the radial processes, they are believed to have a role in receiving regulatory signals from the surrounding niche (Moss et al., 2016). To analyze interactions between R cells and other cell types in the niche, the area of cell marker co-localization was measured. In general, a greater percentage of radial processes in 12-month-old animals

co-localized with niche cell markers for vasculature, pericytes, and microglia, than in younger mice (Figure 7A-B). In young mice, R cell processes preferentially contacted the vasculature in areas with low pericyte coverage (negative for CD13) (Licht et al., 2020), but co-localization of radial processes with CD13-labeled pericytes was increased at 12 months (Figure 7A-B). Further, the number of contacts with IBA1-labeled microglia increased with age, while interactions between R cells and OPCs remained unchanged (Figure 7A-B).

To further confirm the findings of the randomized microniche analyses, we took a more targeted approach, measuring the volumetric distribution of niche cells radiating out from Nestin-labeled radial processes and KI67-labeled proliferating cells. (Figure 7C). Consistent with R cell contact analyses, we found reduced volumes of blood vessels in the immediate vicinity (<15µm distance) of radial processes with densities being unchanged at further distances in 6-month-old animals. Vascular densities were comparable between 2- and 12-month-old animals across all distances from R cells (Figure 7D). In contrast, the relative volume of microglia around R cell processes was increased across all radii in 6- and 12-month-old mice (Figure 7C). For the environment of proliferating cells, we found that vascular density was markedly reduced in aged animals, while microglia were unchanged across all distances (Figure 7C), suggesting that IBA1-expressing microglia is important to maintain the niche but does not directly affect cell proliferation of neurogenic cells within the DG.

Discussion

We here used tissue 4i with the aim to characterize age-related changes in the number and distribution of a variety of cell types within individual tissue sections of the DG. We show that alterations within the neurogenic niche of the DG occur relatively early in life and identify changes in niche cell composition of the BBB and microenvironments surrounding adult NSCs as putative regulators of neurogenic permissiveness throughout life.

Reduced levels of neurogenesis in the mammalian DG have been associated with age-related cognitive decline and neurodegenerative diseases, such as Alzheimer's disease (Kuhn et al., 1996; Drapeau et al., 2003; Ben Abdallah et al., 2010; Knoth et al., 2010; Boldrini et al., 2018; Moreno-Jimenez et al., 2019; Tobin et al., 2019; Denoth-Lippuner and Jessberger, 2021). Thus, previous work aimed to identify age-dependent changes within neurogenic NSCs and their surrounding niches. A number of cell-intrinsic and extrinsic factors have been identified that appear to mediate the age-related decline in NSC activity (Verbitsky et al., 2004; Hafezi-Moghadam et al., 2007; Leeman et al., 2018; Dulken et al., 2019; Martin-Suarez et al., 2019; Morrow et al., 2020; Vonk et al., 2020; Bedrosian et al., 2021). Further, structural but also functional benefits have been associated with experimentally enhanced neurogenesis in aged mice (Villeda et al., 2011; Katsimpardi et al., 2014; McAvoy et al., 2016; Fan et al., 2017; Ozek et al., 2018; Berdugo-Vega et al., 2020; Horowitz et al., 2020). A critical role for vasculature within the dense vessel network of the DG has been described (Palmer et al., 2000; van Praag et al., 2005; Shen et al., 2019). However, it remained difficult to obtain a

comprehensive view of age-related changes within the DG niche due to the difficulty to combine decisive cellular phenotyping of neurogenic cells with a number of different cell type markers within the same tissue section, a requirement to obtain a more complete picture of what changes indeed occur within or in the direct vicinity of NSCs in the mammalian DG. Using tissue 4i we here show that prominent changes in vascular microarchitecture and contact sites occur early on in life. Interestingly, we found that stem cell showed enhanced contact with pericytes with advancing age. Further, our data indicate that both vascular density but also relative distribution of IBA1-labeled microglia and NG2-labeled oligodendroglia are associated with stem cell maintenance in the aged DG. If those cellular alterations are truly responsible for age-related changes of neurogenesis remain to be tested. Future experiments will aim to selectively manipulate newly identified aspects of niche interactions and composition that were identified here, probing for their functional significance. Together with other omics-based approaches that aim to identify age-dependent changes in the aging brain and within NSCs and their progeny (Shavlakadze et al., 2019; Ximerakis et al., 2019; Ibrayeva et al., 2020), the tissue 4i-based dataset we provide here will contribute to future work with the aim to enhance neurogenesis in aged brains. Tissue 4i-based data will contribute to such efforts by not only allowing for high spatial resolution of obtained expression data within complex tissues but also allowing for the characterization of interactions in the three-dimensional space, which is at this time a unique feature of tissue 4i.

We here used 18 different antibodies to label identical tissue sections. However, that number may be easily scaled up when required. We show that

tissue 4i is applicable to a variety of mouse and human tissues, indicating its potential use in basically all tissues and organs. Thus, tissue 4i will be useful to analyse a plethora of tissues and may turn out to be especially useful when only limited tissues/cells are available. For instance, it is a current fundamental limitation in clonal lineage tracing experiments that daughter cells cannot be definitely phenotyped. Rather, current limitations only allow for exclusion-based phenotyping, at least when starter/mother cells can generate a diverse set of daughter cell fates (e.g., a cell expresses protein X and Y but not Z; because only X and Y can be combined for analysis within a single stain, the negativity of Z cannot be shown and phenotypic classification needs to rely on exclusion or non-standardized morphological criteria). Thus, to date, all clonal lineages that generate >2 cell types can only be partially phenotyped and diverse cell types cannot be conclusively classified within the exact same clone (Bonaguidi et al., 2011; Pilz et al., 2018). Tissue 4i will overcome that technical limitations in an easy and readily applicable way, allowing for the use of extensively characterized and validated sets of antibodies with indirect immunofluorescence.

We here demonstrate the applicability of iterative immunostaining in tissue sections using tissue 4i, provide a comprehensive dataset of the aging DG with a large set of combined markers, and identify vasculature- and glia-associated changes within the neurogenic niche that may be responsible to mediate the age-related decline of neurogenesis in the mammalian hippocampus.

Materials & Methods

Mice

Animal experiments were approved by the Cantonal Commission for Animal Experimentation of the Canton of Zurich, Switzerland in accordance with national and cantonal regulations. In developing the tissue 4i protocol, brain tissue was collected from male and female C57Bl/6 mice ranging between 2 and 4 months of age. To attain embryonic day (E) 14.5 embryonic samples, daily plug checks were used to estimate the date of conception. Embryos were collected 14 days following the observation of a vaginal plug. For the aging study, C57BL/6J males at 2 (n = 3), 6 (n = 3), and 12 months (n = 3) of age were used. All mice were kept in a 12 hour light/dark cycle with food and water provided *ad libitum*.

Tissue Preparation

For adult tissues, animals were transcardially perfused using a peristaltic pump with cold 0.9% saline solution followed by 4% PFA in phosphate buffer. Brains were collected and post-fixed in 4% PFA at 4ºC for 8 hours. The brains were then cryo-protected in 30% sucrose for two days prior to sectioning. Adult mouse brain tissue was sectioned into 40µm coronal sections on a cryotome (Leica SM2010R). For E14.5 samples, embryonic heads from C57Bl/6 mice were washed in PBS and fixed with 4% PFA overnight. Cryoprotection occurred in two steps, first for 2 days in 15% sucrose followed by 2 days in 30% sucrose, before being flash frozen and embedded in OCT

Compound (Tissue-Tek) using liquid nitrogen. Sectioning was done coronally at 40µm using a cryostat. Sections were collected and washed with PBS to remove remaining OCT before being transferred to cryoprotectant solution (CPS, 25% Ethyleneglycol, 25% Glycerin, 0.1M phosphate buffer). Forebrain-specific organoids derived from human embryonic stem cells (approved by the Kantonale Ethikkomission Zurich and reported to the federal Bundesamt für Gesundheit of Switzerland) were generated as described before (Bowers et al., 2020), and fixed at day 40 in 4% PFA for 15min, embedded in OCT, and flash frozen using liquid nitrogen. Organoids were sectioned at 40µm using a cryostat, sections were collected in PBS. Serial washes with PBS were performed to remove remaining OCT, before being transferred to CPS.

Mounting

Prior to mounting, glass-bottomed 24 well plates (Cellvis P24-1.5H-N) were coated with 1mg/ml PDL (Sigma P6407). 75µl of the PDL solution was transferred into the center of each well and brushed to the edges with a fine paintbrush to ensure total coverage. The plates were rocked on a shaker for five minutes, after which the PDL was collected for reuse. Wells were rinsed three times with deionized water and let dry for at least 2 hours. Tissue sections were washed three times in PBS, loaded into wells containing 500µl 1x PBS, which was subsequently aspirated allowing the tissue to lie flat and dry for approximately 20 minutes until there was no visible liquid remaining around the edges of the sections. The tissue was then rinsed for 30 seconds with 4% PFA and washed in PBS three times for five minutes each. Organoids sections were gently aspirated using a P1000 pipet with a trimmed

tip and transferred into a well of a glass bottomed well plate. The sections were allowed to settle onto the glass before carefully removing the excess liquid and allowing to dry. Mounted organoid sections were additionally fixed with 4% PFA for 15 minutes followed by three washes with PBS. Prior to staining, the sections were washed with the elution buffer three times for 5 minutes as a form of mild antigen retrieval.

Staining

Once mounted, sections were blocked for 1 hour at room temperature in a blocking solution containing PBS with 3% donkey serum, 0.5% triton-X, and 0.025% PFA (PBS++). Sections were incubated in the primary antibodies (Supplemental Table 1), diluted in the blocking solution, for between two to four nights, depending on the efficacy of the antibodies, shaking at 4ºC. Following the primary antibody incubations, the tissue was washed twice with PBS for 5 minutes and then blocked with PBS++ for one hour at room temperature. Sections were incubated with secondary antibodies, diluted at a ratio of 1:250 along with DAPI at 1:1000 in PBS++, for 3 hours shaking at room temperature, after which the tissue was washed three times with PBS for five minutes. Once the secondary antibody solutions were added all liquid handling was conducted in low light until the antibodies were eluted to reduce the chance of fluorophore crosslinking. The imaging buffer was added at least five minutes prior to imaging to ensure penetrance of the tissue.

Imaging

Before imaging, fresh imaging buffer was prepared by dissolving 0.7M N-Acetyl-Cystein in 0.2M phosphate buffer, using 10M NaOH to adjust the pH to 7.40. Approximately 500µl of the imaging buffer was added each well. All 4i images were taken on a Zeiss LSM800 confocal laser-scanning microscope. Images from tile scans were exported using Carl Zeiss ZEN Blue software and stitched using Fiji (Schindelin et al., 2012). For the aging study, DG images were taken at 20x magnification and composed of tile regions with 10 tiles (5x2), with a pixel resolution of 1024 x 1024 per tile with 16-bit pixel depth. High-resolution close-ups were acquired at 40x magnification with a pixel resolution of 2048 x 2048. All acquisitions were done with bi-directional scanning with a pixel dwell time of 2.06µs. All images will be deposited at the Image Data Resource (https://idr.openmicroscopy.org), allowing for further analyses.

Elution

A stock solution containing 0.5M L-Glycine, 3M Urea, and 3M Guanidine hydrochloride was prepared and kept at 4ºC. Prior to elution, 0.07M (0.02g/ml) TCEP-HCl was added to a volume of the stock solution determined by multiplying the number of wells by the working volume of 150µl by three washes. The pH of the buffer was then lowered to 2.5 using 5M HCl. The tissue was first rinsed with dH_2O, then 150µl of dH_2O followed by 150µl of the elution buffer was added to each well, shaken for 5 minutes and repeated for a total of three washes. After elution the tissue was washed three times for

five minutes in PBS, after which the blocking step for the next round of IF could be started.

Image Alignment

To achieve accurate alignment between rounds of staining, images were registered using consistent DAPI intensity patterns. At a high digital zoom, the x, and y coordinates, as well as the stack position of pixels in DAPI puncta that were recognizable across cycles were measured. Images were transformed in the x, and y planes to align to the image from the first round, with the canvas size being adjust so no image cropped and data was lost. For alignment in the z-plane, slices were added or subtracted to the image stack accordingly.

Antigenicity Test

Brain sections from 2-month-old mice were mounted and stained for HOPX, SOX2, and IBA1. Regions of the DG were imaged with a Zeiss LSM800 confocal laser-scanning microscope. The sections were then subjected to elution washes and imaged again to confirm the loss of signal. Following imaging, six rounds of elution washes (3x 5min) were performed before staining the sections again for HOPX, SOX2, and IBA1. ROIs were drawn around positive cells and fluorescent intensities were measured in the same cells from the two rounds of staining and correlated.

Image Analysis

Cell Counting: R cells were defined by HOPX^{+}/SOX2^{+} soma with a clear vertical process that was also GFAP^{+} and S100β^{-}. Regions of interest were created outlining the cell soma using the polygon selection tool in Fiji, which were saved and later used to measure fluorescent intensities of stem cell markers HOPX, and MT3, the intensity of the nuclear envelope protein LaminB1, as well as checking for the presence of the cell cycle marker KI67. Intensity measures were normalized to the background intensity, which was averaged from five ROIs per slice containing no positive cells within the GCL. Cells were normalized to the background of the representative of the slice in which the cells were measured to account for any gradient in fluorescent intensity caused by unequal antibody penetrance. Non-radial glia-like (NR) cells in cell cycle were identified by being KI67^{+} and located within the lower granular cell layer or SGZ extending approximately 20μm beyond the hilar edge of the GCL. Immature neurons were counted using DCX. Positive cells had a clear ring of non-nuclear staining that encircled a significant majority of the cell (approx. 75%). Glial cell types; astrocytes, microglia, and oligodendrocytes were identified as being S100β+, IBA1+, or NG2+ respectively. Cells were counted throughout the entire images using the Cell Counter plugin in Fiji using localization identifiers for the ML, hilus/CA3, and the supra and infrapyramidal blades of the GCL. The fluorescent intensity of LaminB1 was measured in R cells, immature neurons, and PV interneurons using the ROIs generated during cell counting. For glial cell types, 100 cells were selected at random throughout the imaged hippocampal structures and somatic ROIs were drawn. To ensure accurate measurement, if necessary,

ROIs were adjusted to better fit the LaminB1 outline. Intensity measures were normalized to the background, which was averaged from five ROIs per slice throughout the tissue containing no positive signal. Like with the RGL markers, normalization was slice specific to account for a gradient in intensity across the z-plane.Vasculature dimensions: All measures of vasculature dimensions were conducted using CollagenIV staining. Blood vessel paths were traced and measured using the Simple Neurite Tracer plugin in Fiji and the total length was normalized to the tissue volume. To estimate the vasculature network complexity, Strahler analysis was run to count the number paths at respective branching orders. To calculate vasculature density, volumes were generated based on Cavalieri's principle, summing the area of blood vessels in each slice of an image stack and dividing by the tissue volume. Vasculature areas were measured by applying a 3D gaussian blur with pixel radii of 2, 2, and 1.5 in the x, y, and z directions respectively, thresholding at a fluorescence intensity of 1500, followed by two binary erosions to generate an accurate binary representation of the CollagenIV staining.

Cellular interactions: Cellular interactions were estimated by measuring the area of co-localization of cell markers on vasculature and RGL processes. RGL processes were manually isolated from vasculature in Nestin stains by outlining Nestin+ processes into an ROI and clearing the outside. Binary representations were created the same as was done for CollagenIV for CD13, GFAP, and the isolated Nestin processes with thresholding at lower intensity limits of 1800, 5250, and 2000 respectively. For NG2, IBA1, and s100β, a median filter with a radius of 2 pixels was applied and thresholds were applied at 5500, 2000, and 8500 respectively. ROIs were generated by creating

selections around the binary CollagenIV and Nestin, which were then applied to the other stains, measuring the area of positive pixels within the ROIs. The measured areas were normalized to the total ROI areas to get percent of coverage.

Randomized niche mapping: Binary representations of DCX, HOPX, SOX2, PV, ARC, and KI67 were generated in the same manner as CollagenIV with thresholds set at 2500, 2200, 1600, 4300, 2500, and 2000 respectively. Arc and Ki67 required additional processing to remove remaining background elements. Particle analysis was run to select all for positive cells using a lower area limit of 25μm for ARC, and 15μm for Ki67. ROIs were saved and used to draw the cells onto a blank canvas. To generate randomized sample regions, ROIs were created around the GCL using maximum z-projections of DAPI stains, which was then overlaid and filled in white on a blank image. A second equivalent blank image was subdivided by drawing vertical white bars extending the height of the canvas with a width of 1 pixel, spaced 160 pixels apart, equivalent to 50μm in the microscope image scale. The filled representation of the GCL was multiplied with the image containing the bars resulting in an image with white bars spaced 160 pixels apart, fit to the shape and spanning the width of the blades of the GCL. ROIs were created for each bar individually by particle analysis. On a blank canvas, the bars were filled and an intensity gradient distance map was generated around it. The pixels in the bar had an intensity value of 0, with intensities increasing by 1 with each pixel radiating away from the origin until a value of 255. The binary representations of ARC, CD13, CollagenIV, DCX, GFAP, HOPX, IBA1, Ki67, Nestin, NG2, PV, SOX2, and S100β, which were divided by 255 so the new

intensity value was 1. The binary distance maps for each bar was multiplied against the divided binary images created an image with 8-bit intensity profile representative of the distance from the point of origin. Analyzing the histogram of the resulting images provided the areas and spatial distribution of positive signal for each stain within the distance map. Areas of stains were summed within the distance maps to up to a 160pixel (50μm) radius, which provided adequate and contiguous sampling of the GCL, bordering areas of the hilus, and inner ML. The areas were also summed across the z-stack creating volumes. These were normalized by dividing by the total volume sampled by the distance map and reported as a percentage.

Targeted niche mapping: Distance maps were generated around the Nestin-positive R cell processes, and proliferating cells, and measured against the binary representations of cells the same as was done for the randomized probing. Nestin-labeled R cell processes were measured as a whole per section. Ki67+ cells were isolated using particle analysis on the maximum intensity z-projection. Regions of interest were created around the cells and individually applied to the 3D binary to clear signal outside of the cell of interest. Stain volumes were binned at 5μm intervals and divided by the total measured volume and reported as percent coverage.

Statistical analyses

To assess preservation of antigenicity Pearson correlations were performed on the normalized intensity values of isolated cells. Unpaired t-tests were used to compare counted cell densities, as well as quiescent cell marker and LaminB1 intensities of DCX-labeled immature neurons and PV interneurons

between the 2- and 12-month groups. The standard deviations between age groups were significantly different for the intensities of LaminB1 in R cells, IBA1-labeled microglia, and S100β-positive astrocytes so they were compared using Welch's t-tests. One-way ANOVAs were performed to assess differences between ages in vascular densities, blood vessel coverage, randomized microniche volumes, and stem cell contact measures. These analyses were followed by *post hoc* Tukey's multiple comparisons tests. When data failed the Brown-Forsythe test for equal variances, Welch's ANOVA tests were run with Dunnett's T3 multiple comparisons. For the microniche volumetric measures, Games-Howell's multiple comparisons were used to account for the large group sizes. In comparing spots identified as young and old, Nestin high and low, and KI67 positive and negative, multiple unpaired t-tests were performed with Holms-Sidak correction for multiple comparisons. Microenvironments surrounding radial processes and proliferating cells were analyzed using mixed-effects model analysis and Tukey's multiple comparisons tests.

Acknowledgments

This work was supported by the European Research Council (STEMBAR to S.J., ERC-2019-AdG-885579 to L.P.), the Swiss National Science Foundation (BSCGI0_157859 and 310030_196869 to S.J.; 310030_192622 to L.P.), and the Zurich Neuroscience Center. We thank P. Eugster for analytical help, G. Pilz for conceptual input and advice, and A. Denoth-Lippuner and D.C. Lie for comments on the manuscript.

Author Contributions

J.D.C. performed experiments, analyzed data, and co-wrote the manuscript. J.S.D.C., G.G., L.P., D.G.B. shared unpublished protocols, reagents, tissues. S.J. developed the concept and co-wrote the manuscript.

Declaration of interests

L.P. and G.G. are inventors on a patent related to 4i technology (WO2019207004A1). The other authors declare no competing interests.

References

Bedrosian TA, Houtman J, Eguiguren JS, Ghassemzadeh S, Rund N, Novaresi NM, Hu L, Parylak SL, Denli AM, Randolph-Moore L, Namba T, Gage FH, Toda T (2021) Lamin B1 decline underlies age-related loss of adult hippocampal neurogenesis. The EMBO journal 40:e105819.

Bell RD, Winkler EA, Sagare AP, Singh I, LaRue B, Deane R, Zlokovic BV (2010) Pericytes control key neurovascular functions and neuronal phenotype in the adult brain and during brain aging. Neuron 68:409-427.

Ben Abdallah NM, Slomianka L, Vyssotski AL, Lipp HP (2010) Early age-related changes in adult hippocampal neurogenesis in C57 mice. Neurobiology of aging 31:151-161.

Berdugo-Vega G, Arias-Gil G, Lopez-Fernandez A, Artegiani B, Wasielewska JM, Lee CC, Lippert MT, Kempermann G, Takagaki K, Calegari F (2020) Increasing neurogenesis refines hippocampal activity rejuvenating navigational learning strategies and contextual memory throughout life. Nat Commun 11:135.

Berg DA, Su Y, Jimenez-Cyrus D, Patel A, Huang N, Morizet D, Lee S, Shah R, Ringeling FR, Jain R, Epstein JA, Wu QF, Canzar S, Ming GL, Song H, Bond AM (2019) A Common Embryonic Origin of Stem Cells Drives Developmental and Adult Neurogenesis. Cell 177:654-668 e615.

Bin Imtiaz MK, Jaeger BN, Bottes S, Machado RAC, Vidmar M, Moore DL, Jessberger S (2021) Declining lamin B1 expression mediates age-dependent decreases of hippocampal stem cell activity. Cell Stem Cell.

Boldrini M, Fulmore CA, Tartt AN, Simeon LR, Pavlova I, Poposka V, Rosoklija GB, Stankov A, Arango V, Dwork AJ, Hen R, Mann JJ (2018) Human Hippocampal Neurogenesis Persists throughout Aging. Cell Stem Cell 22:589-599 e585.

Bonaguidi MA, Wheeler MA, Shapiro JS, Stadel RP, Sun GJ, Ming GL, Song H (2011) In Vivo Clonal Analysis Reveals Self-Renewing and Multipotent Adult Neural Stem Cell Characteristics. Cell.

Bottes S, Jaeger BN, Pilz GA, Jorg DJ, Cole JD, Kruse M, Harris L, Korobeynyk VI, Mallona I, Helmchen F, Guillemot F, Simons BD, Jessberger S (2021) Long-term self-renewing stem cells in the adult mouse hippocampus identified by intravital imaging. Nat Neurosci 24:225-233.

Bowers M, Liang T, Gonzalez-Bohorquez D, Zocher S, Jaeger BN, Kovacs WJ, Rohrl C, Cramb KML, Winterer J, Kruse M, Dimitrieva S, Overall RW, Wegleiter T, Najmabadi H, Semenkovich CF, Kempermann G, Foldy C, Jessberger S (2020) FASN-Dependent Lipid Metabolism Links Neurogenic Stem/Progenitor Cell Activity to Learning and Memory Deficits. Cell Stem Cell 27:98-109 e111.

Burgess DJ (2019) Spatial transcriptomics coming of age. Nat Rev Genet 20:317.

Burke B, Stewart CL (2013) The nuclear lamins: flexibility in function. Nat Rev Mol Cell Biol 14:13-24.

Decalf J, Albert ML, Ziai J (2019) New tools for pathology: a user's review of a highly multiplexed method for in situ analysis of protein and RNA expression in tissue. J Pathol 247:650-661.

Denoth-Lippuner A, Jessberger S (2021) Formation and integration of new neurons in the adult hippocampus. Nature reviews.

Drapeau E, Mayo W, Aurousseau C, Le Moal M, Piazza PV, Abrous DN (2003) Spatial memory performances of aged rats in the water maze predict levels of hippocampal neurogenesis. Proceedings of the National Academy of Sciences of the United States of America 100:14385-14390.

Dulken BW, Buckley MT, Navarro Negredo P, Saligrama N, Cayrol R, Leeman DS, George BM, Boutet SC, Hebestreit K, Pluvinage JV, Wyss-Coray T, Weissman IL, Vogel H, Davis MM, Brunet A (2019) Single-cell analysis reveals T cell infiltration in old neurogenic niches. Nature 571:205-210.

Ermolaeva M, Neri F, Ori A, Rudolph KL (2018) Cellular and epigenetic drivers of stem cell ageing. Nat Rev Mol Cell Biol 19:594-610.

Fan X, Wheatley EG, Villeda SA (2017) Mechanisms of Hippocampal Aging and the Potential for Rejuvenation. Annual review of neuroscience 40:251-272.

Fuchs E, Segre JA (2000) Stem cells: a new lease on life. Cell 100:143-155.

Gage FH (2019) Adult neurogenesis in mammals. Science (New York, NY 364:827-828.

Giesen C, Wang HA, Schapiro D, Zivanovic N, Jacobs A, Hattendorf B, Schuffler PJ, Grolimund D, Buhmann JM, Brandt S, Varga Z, Wild PJ, Gunther D, Bodenmiller B (2014) Highly multiplexed imaging of tumor tissues with subcellular resolution by mass cytometry. Nature methods 11:417-422.

Gut G, Herrmann MD, Pelkmans L (2018) Multiplexed protein maps link subcellular organization to cellular states. Science (New York, NY 361.

Hafezi-Moghadam A, Thomas KL, Wagner DD (2007) ApoE deficiency leads to a progressive age-dependent blood-brain barrier leakage. American journal of physiology Cell physiology 292:C1256-1262.

Harris L, Rigo P, Stiehl T, Gaber ZB, Austin SHL, Masdeu MDM, Edwards A, Urban N, Marciniak-Czochra A, Guillemot F (2021) Coordinated changes in cellular behavior ensure the lifelong maintenance of the hippocampal stem cell population. Cell Stem Cell.

Horowitz AM, Fan X, Bieri G, Smith LK, Sanchez-Diaz CI, Schroer AB, Gontier G, Casaletto KB, Kramer JH, Williams KE, Villeda SA (2020)

Blood factors transfer beneficial effects of exercise on neurogenesis and cognition to the aged brain. Science (New York, NY 369:167-173.

Ibrayeva A, Bay M, Pu E, Jörg D, Peng L, Jun H, Zhang N, Aaron D, Lin C, Resler G, Hidalgo A, Jang M-H, Simons BD, Bonaguidi MA (2020) Early Stem Cell Aging in the Mature Brain. bioRxiv:654608.

Kalamakis G et al. (2019) Quiescence Modulates Stem Cell Maintenance and Regenerative Capacity in the Aging Brain. Cell 176:1407-1419 e1414.

Katsimpardi L, Litterman NK, Schein PA, Miller CM, Loffredo FS, Wojtkiewicz GR, Chen JW, Lee RT, Wagers AJ, Rubin LL (2014) Vascular and neurogenic rejuvenation of the aging mouse brain by young systemic factors. Science (New York, NY 344:630-634.

Knoth R, Singec I, Ditter M, Pantazis G, Capetian P, Meyer RP, Horvat V, Volk B, Kempermann G (2010) Murine features of neurogenesis in the human hippocampus across the lifespan from 0 to 100 years. PLoS ONE 5:e8809.

Kronenberg G, Reuter K, Steiner B, Brandt MD, Jessberger S, Yamaguchi M, Kempermann G (2003) Subpopulations of proliferating cells of the adult hippocampus respond differently to physiologic neurogenic stimuli. The Journal of comparative neurology 467:455-463.

Kuhn HG, Dickinson-Anson H, Gage FH (1996) Neurogenesis in the dentate gyrus of the adult rat: age-related decrease of neuronal progenitor proliferation. J Neurosci 16:2027-2033.

Leeman DS, Hebestreit K, Ruetz T, Webb AE, McKay A, Pollina EA, Dulken BW, Zhao X, Yeo RW, Ho TT, Mahmoudi S, Devarajan K, Passegue E, Rando TA, Frydman J, Brunet A (2018) Lysosome activation clears aggregates and enhances quiescent neural stem cell activation during aging. Science (New York, NY 359:1277-1283.

Licht T, Sasson E, Bell B, Grunewald M, Kumar S, Kreisel T, Ben-Zvi A, Keshet E (2020) Hippocampal neural stem cells facilitate access from circulation via apical cytoplasmic processes. Elife 9.

Lin JR, Izar B, Wang S, Yapp C, Mei S, Shah PM, Santagata S, Sorger PK (2018) Highly multiplexed immunofluorescence imaging of human tissues and tumors using t-CyCIF and conventional optical microscopes. Elife 7.

Martin-Suarez S, Valero J, Muro-Garcia T, Encinas JM (2019) Phenotypical and functional heterogeneity of neural stem cells in the aged hippocampus. Aging cell 18:e12958.

McAvoy KM, Scobie KN, Berger S, Russo C, Guo N, Decharatanachart P, Vega-Ramirez H, Miake-Lye S, Whalen M, Nelson M, Bergami M, Bartsch D, Hen R, Berninger B, Sahay A (2016) Modulating Neuronal Competition Dynamics in the Dentate Gyrus to Rejuvenate Aging Memory Circuits. Neuron 91:1356-1373.

Moncada R, Barkley D, Wagner F, Chiodin M, Devlin JC, Baron M, Hajdu CH, Simeone DM, Yanai I (2020) Integrating microarray-based spatial transcriptomics and single-cell RNA-seq reveals tissue architecture in pancreatic ductal adenocarcinomas. Nature biotechnology 38:333-342.

Moore DL, Pilz GA, Arauzo-Bravo MJ, Barral Y, Jessberger S (2015) A mechanism for the segregation of age in mammalian neural stem cells. Science (New York, NY 349:1334-1338.

Moreno-Jimenez EP, Flor-Garcia M, Terreros-Roncal J, Rabano A, Cafini F, Pallas-Bazarra N, Avila J, Llorens-Martin M (2019) Adult hippocampal neurogenesis is abundant in neurologically healthy subjects and drops sharply in patients with Alzheimer's disease. Nature medicine 25:554-560.

Morrison SJ, Spradling AC (2008) Stem cells and niches: mechanisms that promote stem cell maintenance throughout life. Cell 132:598-611.

Morrow CS, Porter TJ, Xu N, Arndt ZP, Ako-Asare K, Heo HJ, Thompson EAN, Moore DL (2020) Vimentin Coordinates Protein Turnover at the Aggresome during Neural Stem Cell Quiescence Exit. Cell Stem Cell 26:558-568 e559.

Mosher KI, Schaffer DV (2018) Influence of hippocampal niche signals on neural stem cell functions during aging. Cell and tissue research 371:115-124.

Moss J, Gebara E, Bushong EA, Sanchez-Pascual I, O'Laoi R, El M'Ghari I, Kocher-Braissant J, Ellisman MH, Toni N (2016) Fine processes of Nestin-GFP-positive radial glia-like stem cells in the adult dentate gyrus ensheathe local synapses and vasculature. Proceedings of the

National Academy of Sciences of the United States of America 113:E2536-2545.

Navarro Negredo P, Yeo RW, Brunet A (2020) Aging and Rejuvenation of Neural Stem Cells and Their Niches. Cell Stem Cell 27:202-223.

Ozek C, Krolewski RC, Buchanan SM, Rubin LL (2018) Growth Differentiation Factor 11 treatment leads to neuronal and vascular improvements in the hippocampus of aged mice. Sci Rep 8:17293.

Palmer TD, Willhoite AR, Gage FH (2000) Vascular niche for adult hippocampal neurogenesis. The Journal of comparative neurology 425:479-494.

Pilz GA, Bottes S, Betizeau M, Jorg DJ, Carta S, Simons BD, Helmchen F, Jessberger S (2018) Live imaging of neurogenesis in the adult mouse hippocampus. Science (New York, NY 359:658-662.

Schapiro D, Jackson HW, Raghuraman S, Fischer JR, Zanotelli VRT, Schulz D, Giesen C, Catena R, Varga Z, Bodenmiller B (2017) histoCAT: analysis of cell phenotypes and interactions in multiplex image cytometry data. Nature methods 14:873-876.

Schulz D, Zanotelli VRT, Fischer JR, Schapiro D, Engler S, Lun XK, Jackson HW, Bodenmiller B (2018) Simultaneous Multiplexed Imaging of mRNA and Proteins with Subcellular Resolution in Breast Cancer Tissue Samples by Mass Cytometry. Cell Syst 6:25-36 e25.

Seri B, Garcia-Verdugo JM, McEwen BS, Alvarez-Buylla A (2001) Astrocytes give rise to new neurons in the adult mammalian hippocampus. J Neurosci 21:7153-7160.

Shavlakadze T, Morris M, Fang J, Wang SX, Zhu J, Zhou W, Tse HW, Mondragon-Gonzalez R, Roma G, Glass DJ (2019) Age-Related Gene Expression Signature in Rats Demonstrate Early, Late, and Linear Transcriptional Changes from Multiple Tissues. Cell reports 28:3263-3273 e3263.

Shen J, Wang D, Wang X, Gupta S, Ayloo B, Wu S, Prasad P, Xiong Q, Xia J, Ge S (2019) Neurovascular Coupling in the Dentate Gyrus Regulates Adult Hippocampal Neurogenesis. Neuron 103:878-890 e873.

Shin J, Berg DA, Zhu Y, Shin JY, Song J, Bonaguidi MA, Enikolopov G, Nauen DW, Christian KM, Ming GL, Song H (2015) Single-Cell RNA-

Seq with Waterfall Reveals Molecular Cascades underlying Adult Neurogenesis. Cell Stem Cell 17:360-372.

Song J, Olsen RH, Sun J, Ming GL, Song H (2016) Neuronal Circuitry Mechanisms Regulating Adult Mammalian Neurogenesis. Cold Spring Harbor perspectives in biology 8.

Stahl PL et al. (2016) Visualization and analysis of gene expression in tissue sections by spatial transcriptomics. Science (New York, NY 353:78-82.

Tobin MK, Musaraca K, Disouky A, Shetti A, Bheri A, Honer WG, Kim N, Dawe RJ, Bennett DA, Arfanakis K, Lazarov O (2019) Human Hippocampal Neurogenesis Persists in Aged Adults and Alzheimer's Disease Patients. Cell Stem Cell 24:974-982 e973.

van Praag H, Shubert T, Zhao C, Gage FH (2005) Exercise enhances learning and hippocampal neurogenesis in aged mice. J Neurosci 25:8680-8685.

Verbitsky M, Yonan AL, Malleret G, Kandel ER, Gilliam TC, Pavlidis P (2004) Altered hippocampal transcript profile accompanies an age-related spatial memory deficit in mice. Learning & memory (Cold Spring Harbor, NY 11:253-260.

Villeda SA et al. (2011) The ageing systemic milieu negatively regulates neurogenesis and cognitive function. Nature 477:90-94.

Vonk WIM, Rainbolt TK, Dolan PT, Webb AE, Brunet A, Frydman J (2020) Differentiation Drives Widespread Rewiring of the Neural Stem Cell Chaperone Network. Molecular cell 78:329-345 e329.

Wagner J, Rapsomaniki MA, Chevrier S, Anzeneder T, Langwieder C, Dykgers A, Rees M, Ramaswamy A, Muenst S, Soysal SD, Jacobs A, Windhager J, Silina K, van den Broek M, Dedes KJ, Rodriguez Martinez M, Weber WP, Bodenmiller B (2019) A Single-Cell Atlas of the Tumor and Immune Ecosystem of Human Breast Cancer. Cell 177:1330-1345 e1318.

Ximerakis M, Lipnick SL, Innes BT, Simmons SK, Adiconis X, Dionne D, Mayweather BA, Nguyen L, Niziolek Z, Ozek C, Butty VL, Isserlin R, Buchanan SM, Levine SS, Regev A, Bader GD, Levin JZ, Rubin LL (2019) Single-cell transcriptomic profiling of the aging mouse brain. Nat Neurosci 22:1696-1708.

Figures

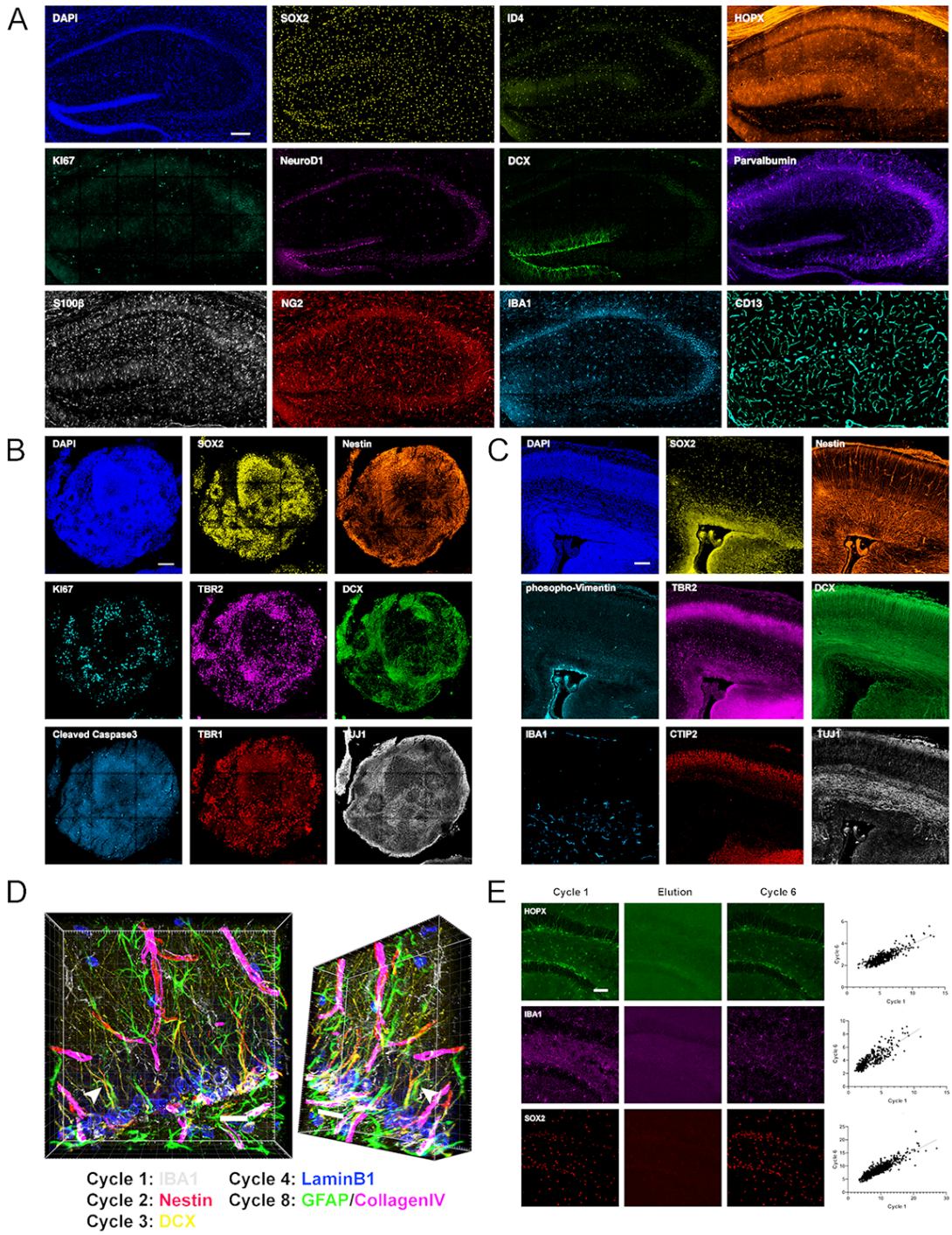

Figure 1. Iterative immunostaining in mouse and human tissue sections.

(A) Shown is an adult mouse dorsal hippocampal section labeled with 11 antibodies, as indicated in the individual panels, acquired over five rounds of tissue 4i. SOX2/ID4/HOPX astrocytes/NSCs; KI67, proliferation;

NeuroD1/DCX, immature neurons; Parvalbumin, interneurons; S100β, astrocytes; NG2, oligodendroglia; IBA1, microglia; CD13, pericytes. Nuclei were counterstained with DAPI. **(B)** A hESC-derived, forebrain organoid section fixed at day 40 in vitro and labeled with eight antibodies, as indicated in the individual panels, over four rounds of tissue 4i. SOX2/Nestin, apical progenitors; KI67, proliferation; TBR2, basal progenitors; DCX, immature neurons; cCaspase3, apoptotic cells; TBR1/TUJ1, neurons. Nuclei were counterstained with DAPI. **(C)** Shown is a cortical section from an E14.5 mouse embryo labeled with eight antibodies, as indicated in the individual panels, over four rounds of tissue 4i. Phopho-Vimentin, intermediate filaments; IBA1, microglia; SOX2/Nestin, astrocytes/NSCs; TBR2, basal progenitors; CTIP2, neurons; DCX/TUJ1, immature neurons. Nuclei were counterstained with DAPI. **(D)** 3D reconstruction of a region in the dorsal DG analyzed with antibodies as indicated, with an arrow highlighting a $Nestin^{+}/GFAP^{+}$ R cell radial process indicating the spatial fidelity of tissue 4i across cycles. **(E)** Examples of HOPX, IBA1, and SOX2 labeling in adult mouse brain sections, with proof of elution efficacy and restaining quality. The normalized fluorescent intensities for each stain were correlated between rounds. For details of statistics please refer to Supplemental Table 1.

Scale bars represent 200μm (A), 100μm (B, C), 25μm (D), 50μm (E).

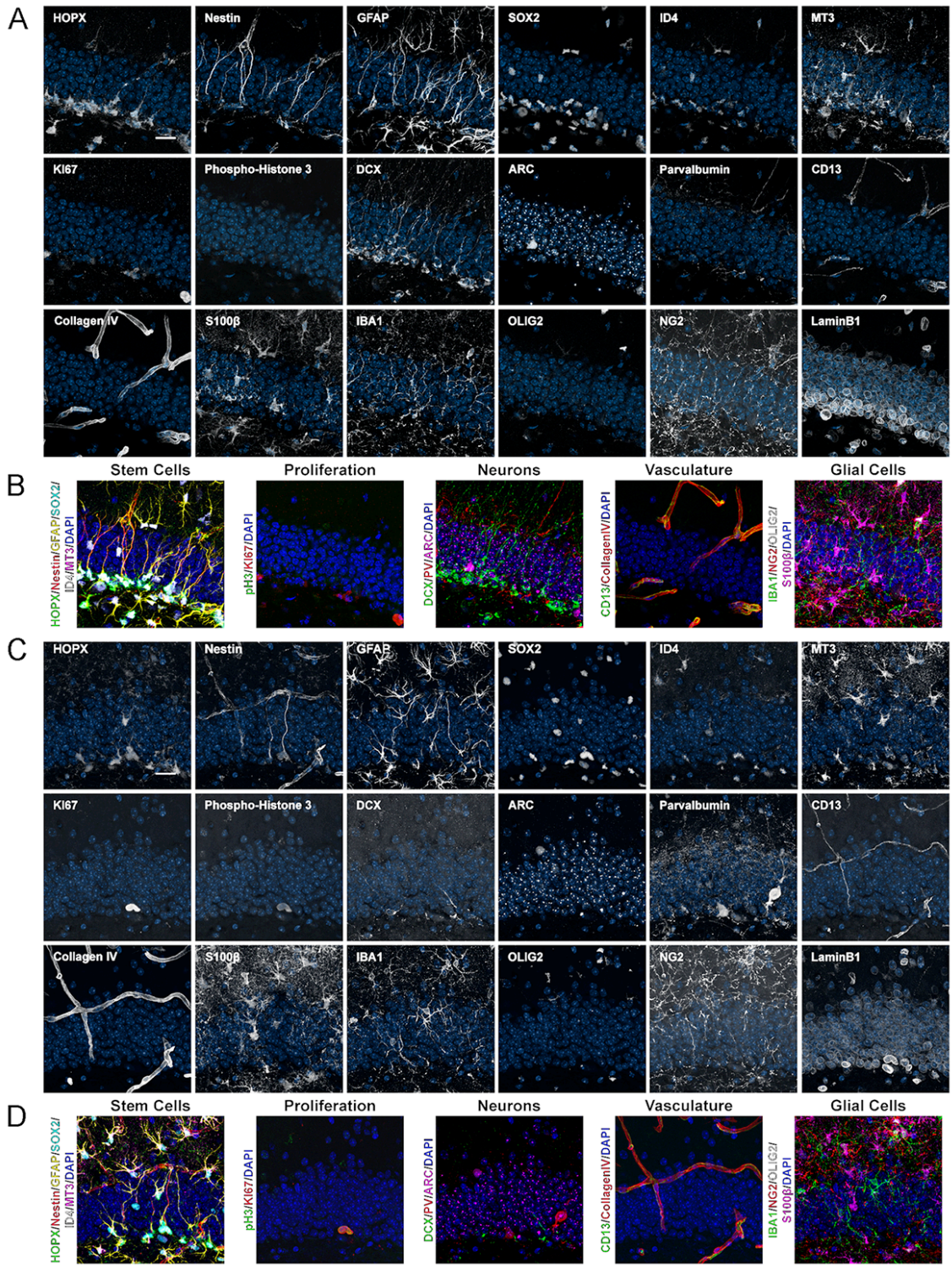

Figure 2. Expression of 18 proteins in the young and aged mouse DG.

(A) Images of 18 proteins labeled in the same area of the DG from a 2-month-old mouse. HOPX/Nestin/GFAP/SOX2/ID4/MT3 astrocytes/NSCs;

KI67/phospho-Histone 3, proliferation; DCX, immature neurons; ARC, mature neurons; Parvalbumin, interneurons; CD13, pericytes; CollagenIV, vasculature; S100β, astrocytes; IBA1, microglia; OLIG2/NG2, oligodendroglia; LaminB1, nuclear lamina. **(B)** shows merged channels for stem cells, proliferation, neurons, vaculature, and glial cells. Nuclei were counterstained with DAPI. **(C)** Images of 18 proteins labeled in the same area of the DG from a 12-month-old mouse. **(D)** shows composites grouping markers based on cell type. Scale bars represent 25μm.

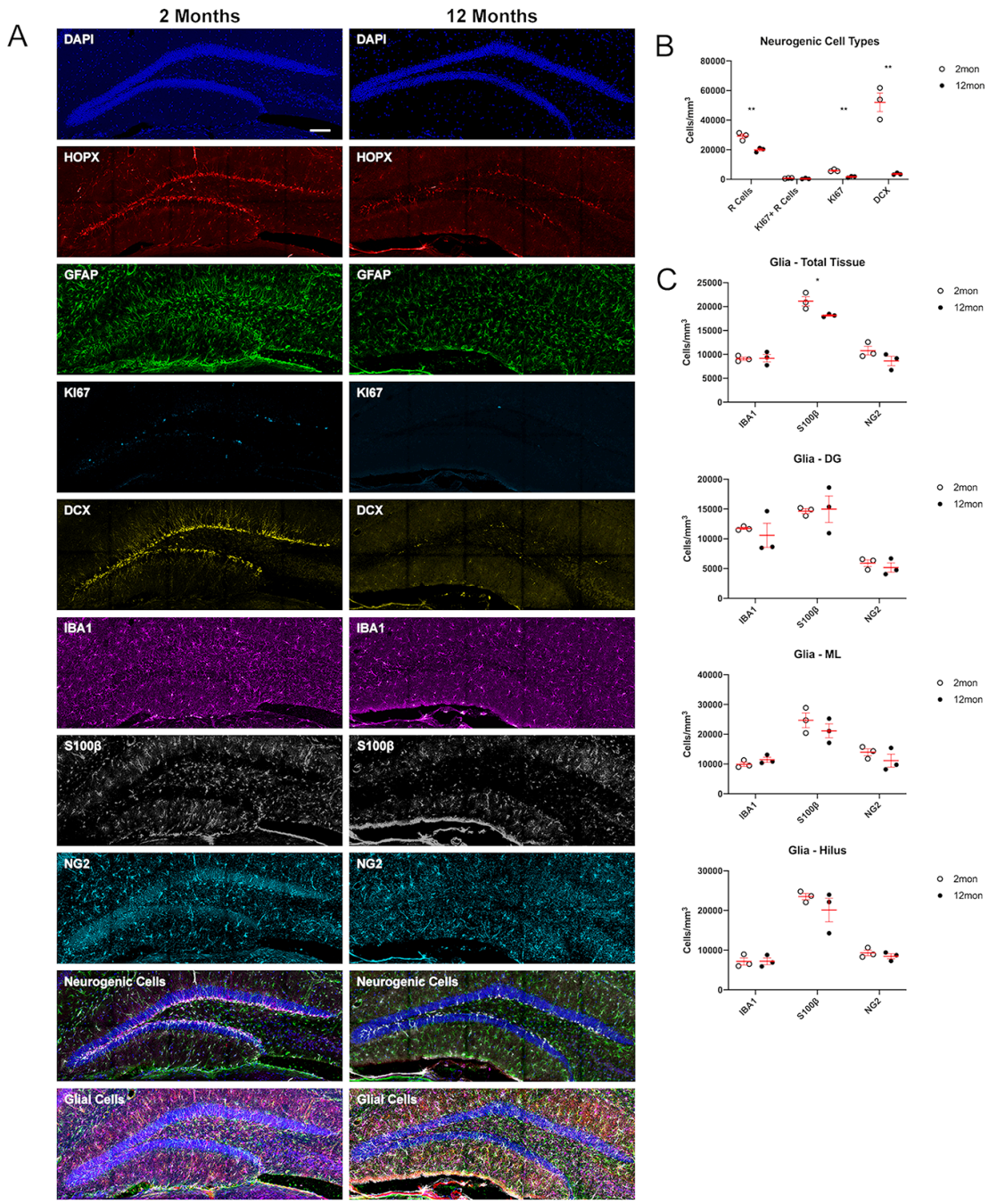

Figure 3. Age-related dynamics of cell populations in the mouse DG.

(A) Example overviews of the same DGs from 2- and 12-month-old mice showing the neurogenic and glial markers used to phenotype cells in population density measures. Nuclei were counterstained with DAPI. **(B)** Density analyses of neurogenic cells in the SGZ, defined as the number of R

cells. For details of statistics please refer to Supplemental Table 1. **(C)** Density analyses of microglia, OPCs, and astrocytes in the total sampled area of the DG, in the granule cell layer, the molecular layer, and hilus. For details of statistics please refer to Supplemental Table 1.

Scale bar represents 100µm. * $p < 0.05$, ** $p < 0.01$

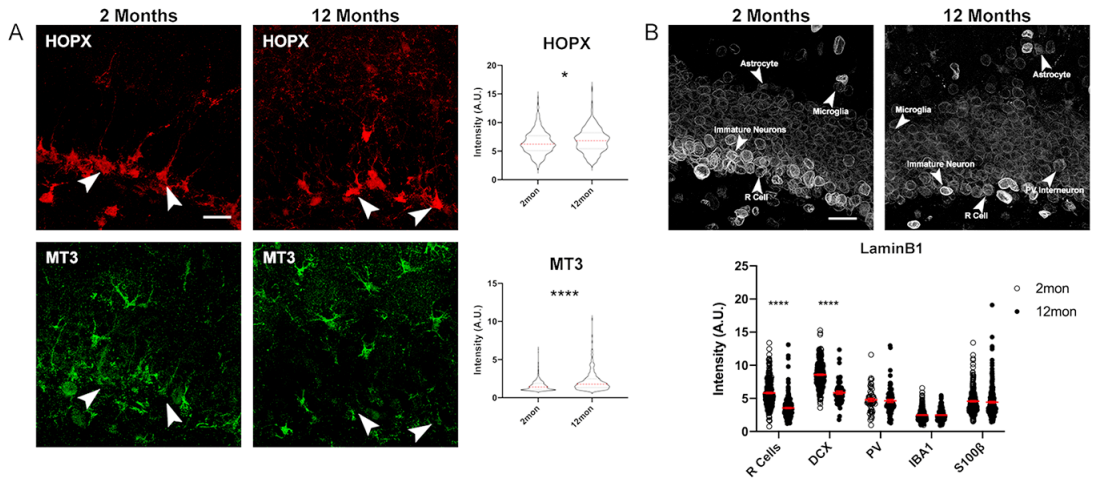

Figure 4. Age-dependent changes of protein expression in the DG.

(A) Representative images of 2- and 12-month-old DG sections labeled with quiescent markers HOPX, and MT3 with quantification of the fluorescent intensities normalized to background. Arrowheads indicate the same cell across stains. For details of statistics please refer to Supplemental Table 1. **(B)** Images showing LaminB1 in DGs from 2 and 12 month old mice with different cell types indicated by arrows with quantification of the fluorescent intensities normalized to background. For details of statistics please refer to Supplemental Table 1.

Scale bars represent 25μm. **** $p < 0.0001$

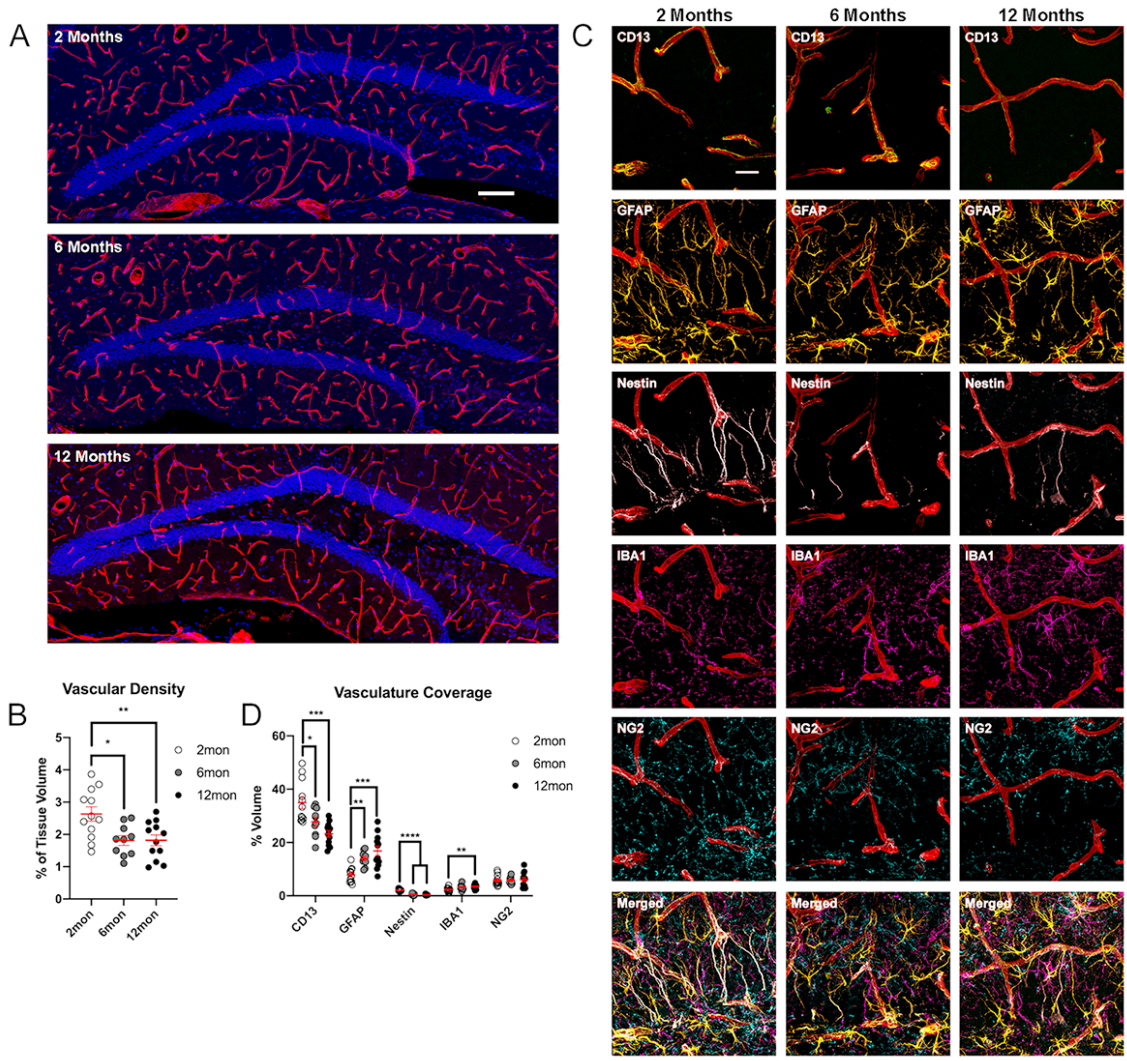

Figure 5. Changes of DG vasculature with age.

(A) Images of CollagenIV+ blood vessels in the DGs at 2, 6 and 12 months. Nuclei were counterstained with DAPI. **(B)** Quantification of vascular density in the DGs of 2, 6 and 12 month old mice. For details of statistics please refer to Supplemental Table 1. **(C)** Representative images showing the interactions of pericytes, glia, and R cells with the vasculature in the DG. **(D)** Quantification of co-localization of pericytes, astrocytes, R cells, microglia, and OPCs with CollagenIV+ represented a percentage of total vascular volume. For details of statistics please refer to Supplemental Table 1.

Scale bars represent 100μm (A), 25μm (C). ** $p < 0.01$, *** $p < 0.001$, **** $p < 0.0001$

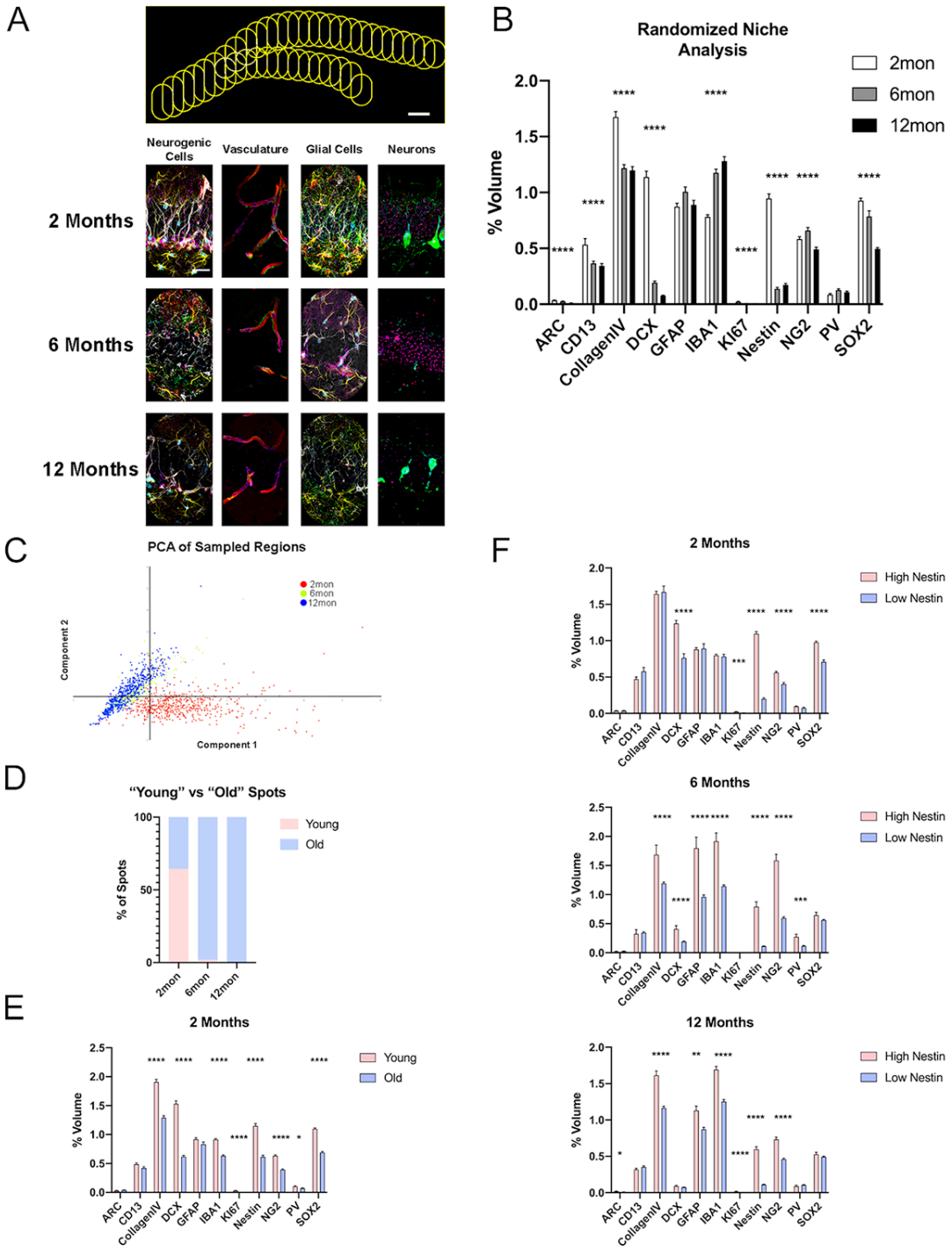

Figure 6. Microniche analysis reveals features of aging neurogenic niche. **(A)** A representative overview of the arrangement of randomized sampling spots, with close up examples of the cellular contents within a single sampled spot for each age group. **(B)** Quantification of volumes of cell types within the

random sampled spots normalized to the sampled area. For details of statistics please refer to Supplemental Table 1.

Scale bars represent 25µm (A, lower panels) and 100µm (upper panel). * $p < 0.05$, ** $p < 0.01$, *** $p < 0.001$, **** $p < 0.0001$

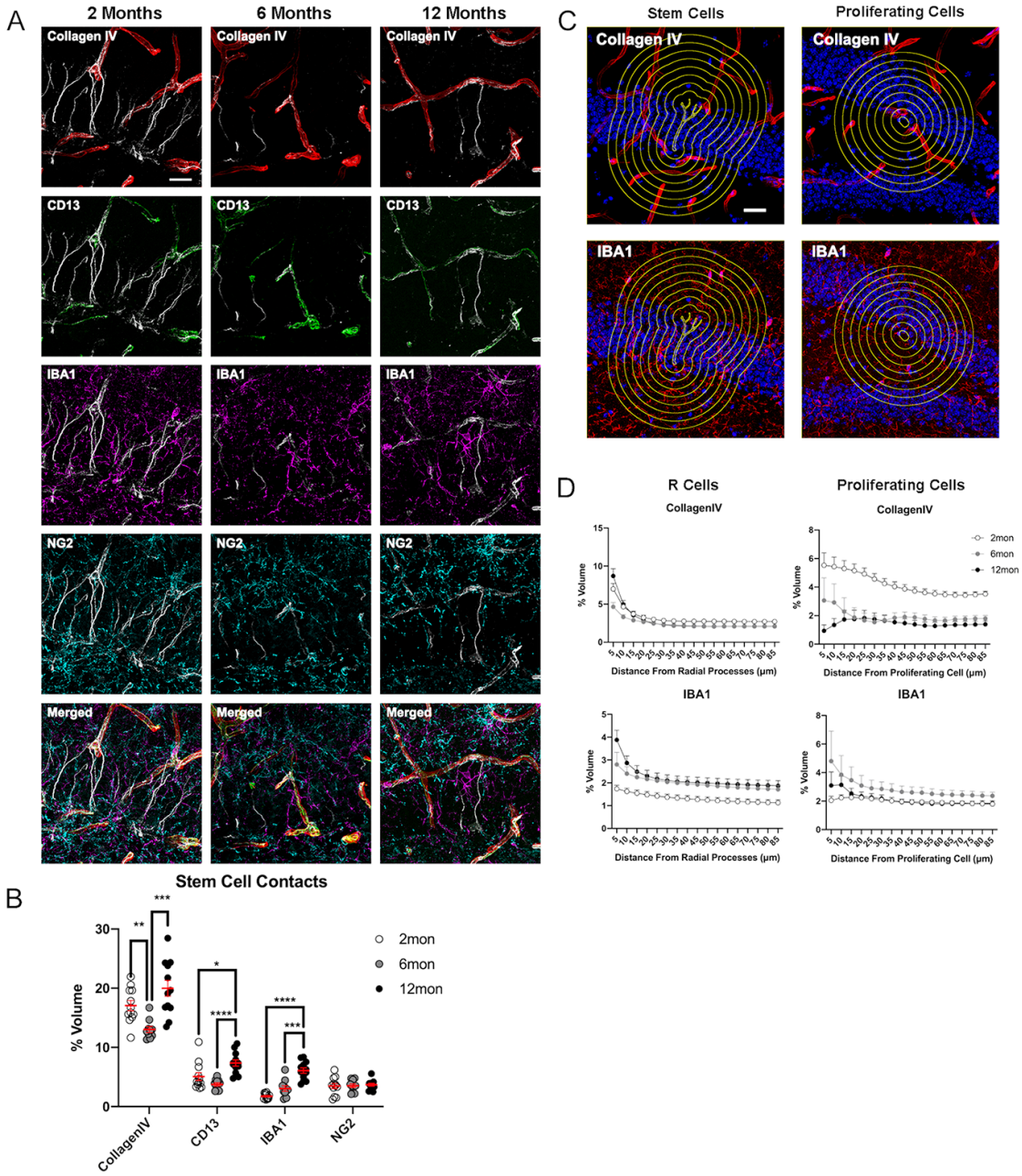

Figure 7. Age-dependent dynamics of the niche surrounding adult stem cells.

(A) Representative images showing the interactions of R cells with vascular and glial cells in the surrounding niche in the DG in 2-, 6-, and 12-month-old mice. **(B)** Quantification of co-localization of blood vessels, pericytes, microglia, and OPCs with CollagenIV+ represented a percentage of total

vascular volume. For details of statistics please refer to Supplemental Table 1. **(C)** Representative images of areas measured for volumes of vasculature and microglia at radiating distances around Nestin-positive R cells and Ki67-positive proliferating cells. **(D)** Quantification of volumes of vasculature and microglia at radiating distances from R cells and Ki67+ proliferating cells For details of statistics please refer to Supplemental Table 1. Scale bars represent 25μm. Scale bar represents 100μm. * $p < 0.05$, ** $p < 0.01$, *** $p < 0.001$, **** $p < 0.0001$

Supplemental figures

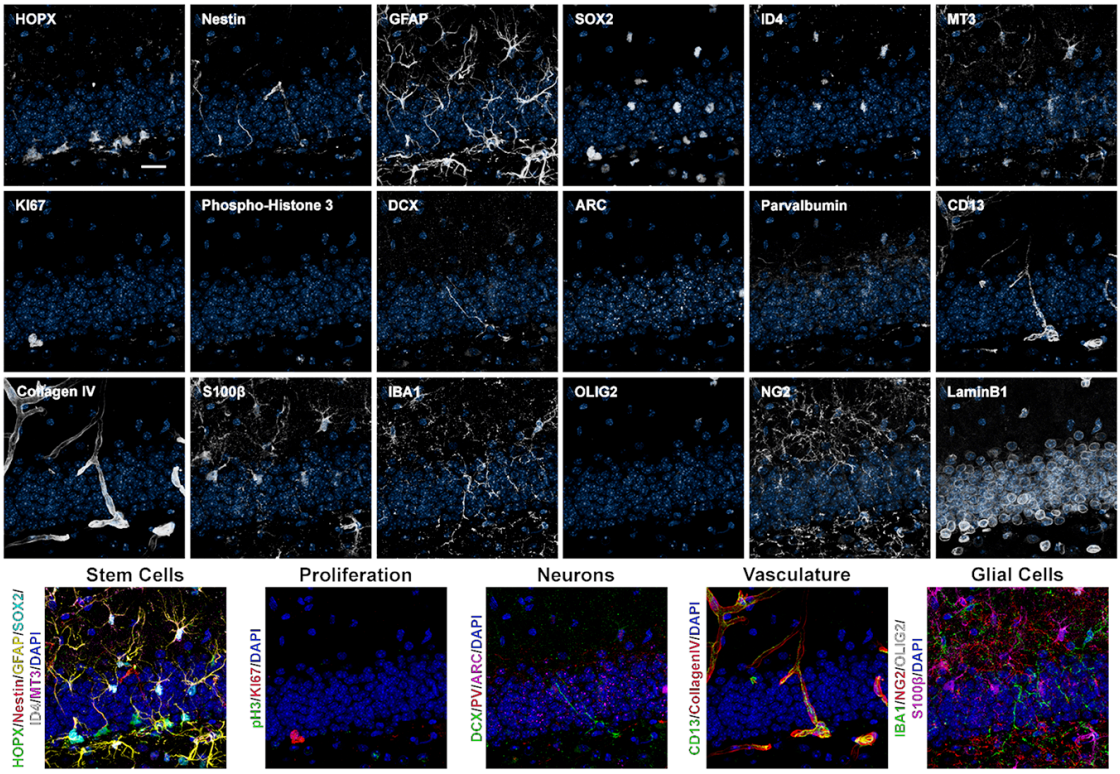

Figure 2 - Supplemental 1

(A) Close up images of the 18 proteins labeled in the same area of the DG from a 6-month-old mouse with composites grouping markers (B) based on cell type. Scale bar represents 25µm.

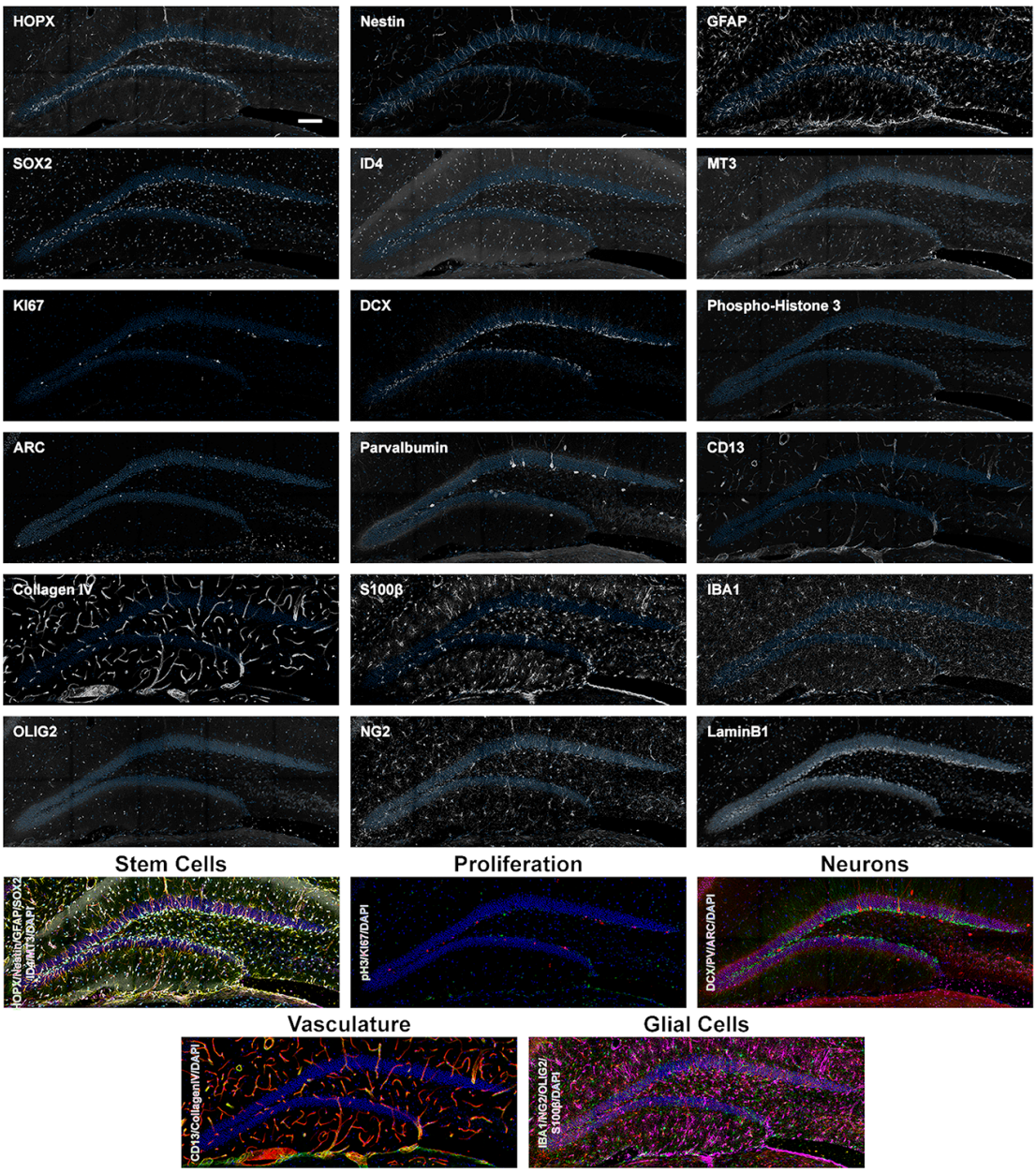

Figure 2 - Supplemental 2

(A) Overview images of the 18 proteins labeled in the same area of the DG from a 2-month-old mouse with composites grouping markers (B) based on cell type. Scale bar represents 100μm.

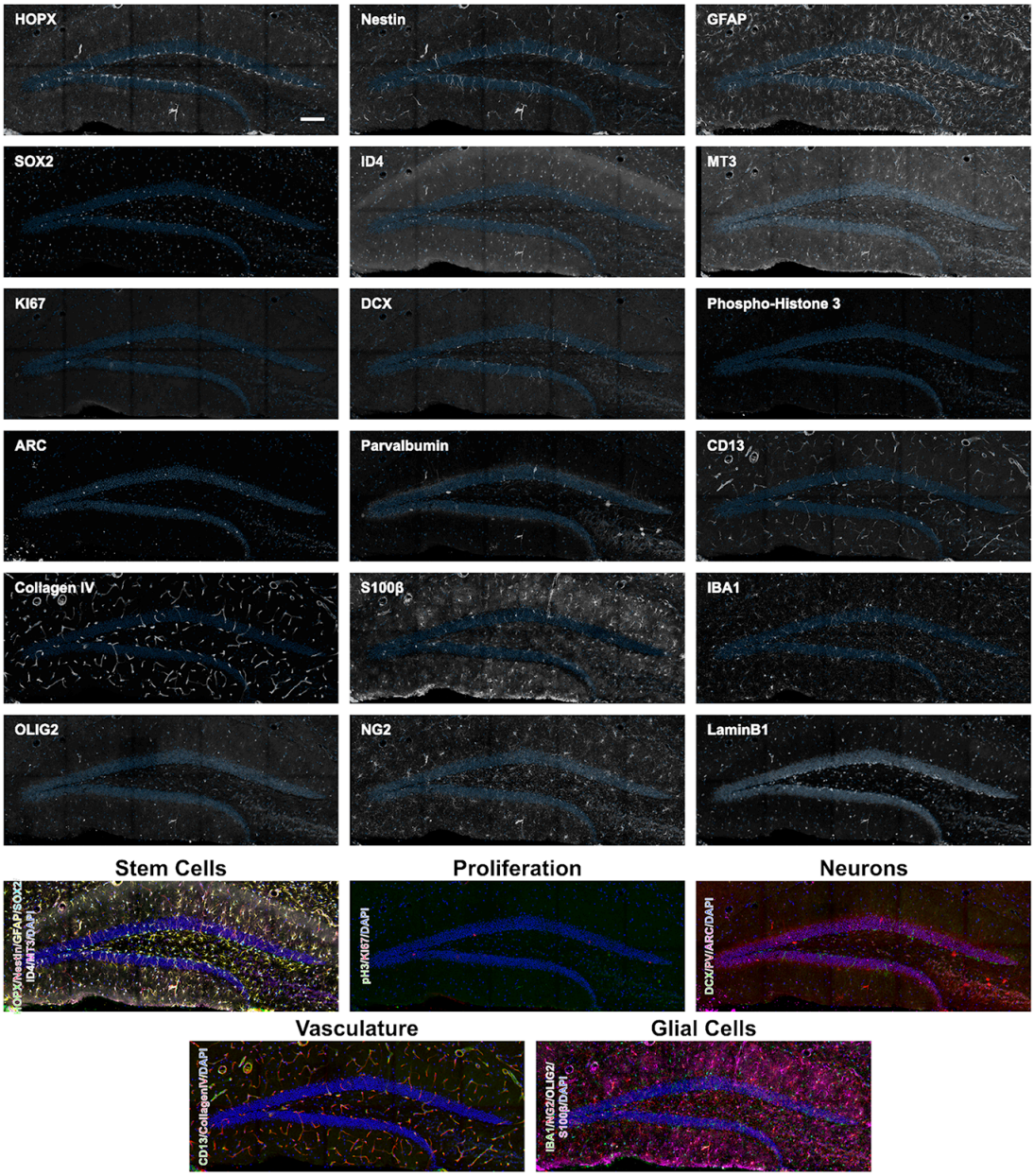

Figure 2 - Supplemental 3

(A) Overview images of the 18 proteins labeled in the same area of the DG from a 12-month-old mouse with composites grouping markers (B) based on cell type. Scale bar represents 100μm

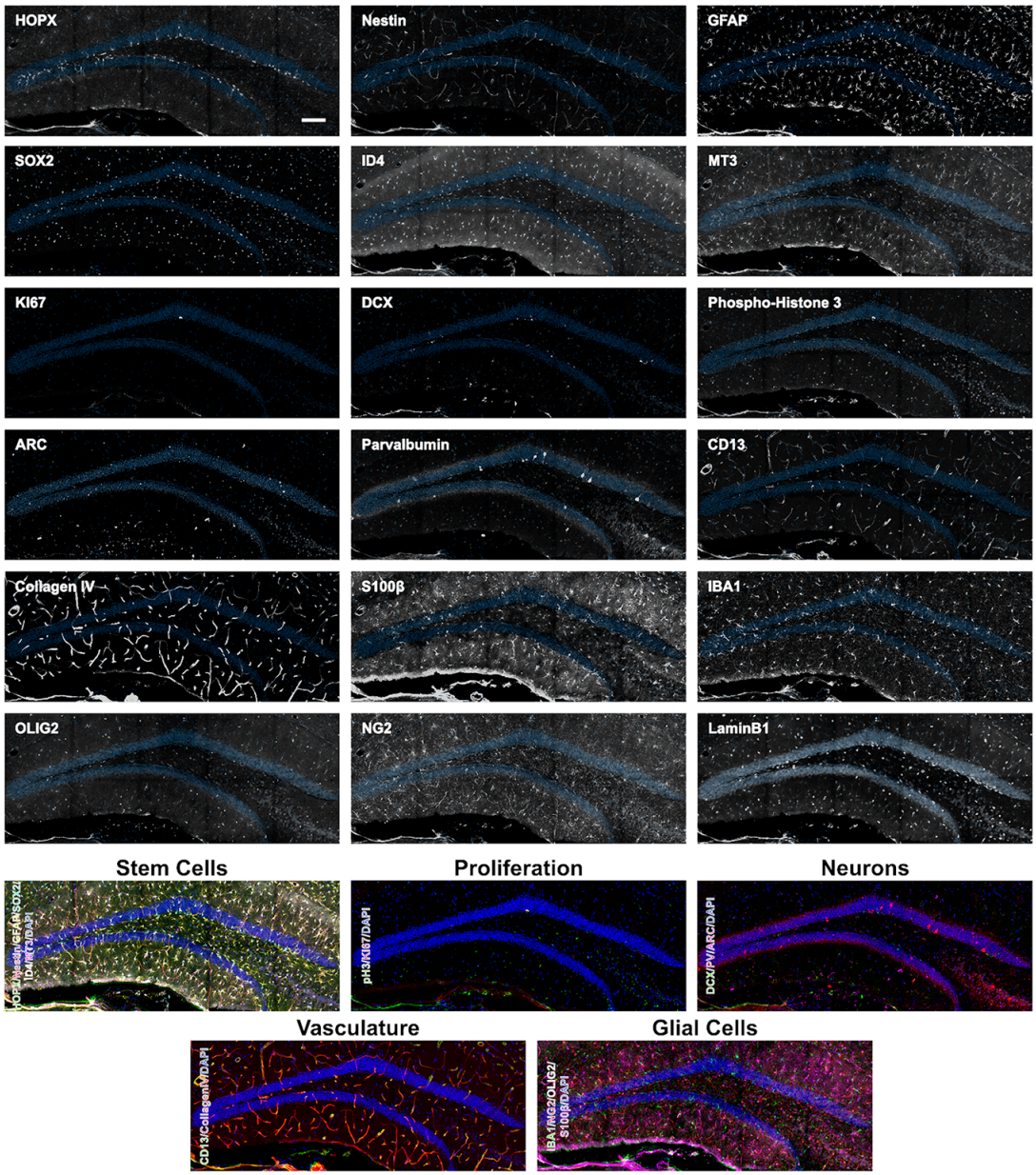

Figure 2 - Supplemental 4

(A) Overview images of the 18 proteins labeled in the same area of the DG from a 6-month-old mouse with composites grouping markers (B) based on cell type. Scale bar represents 100μm

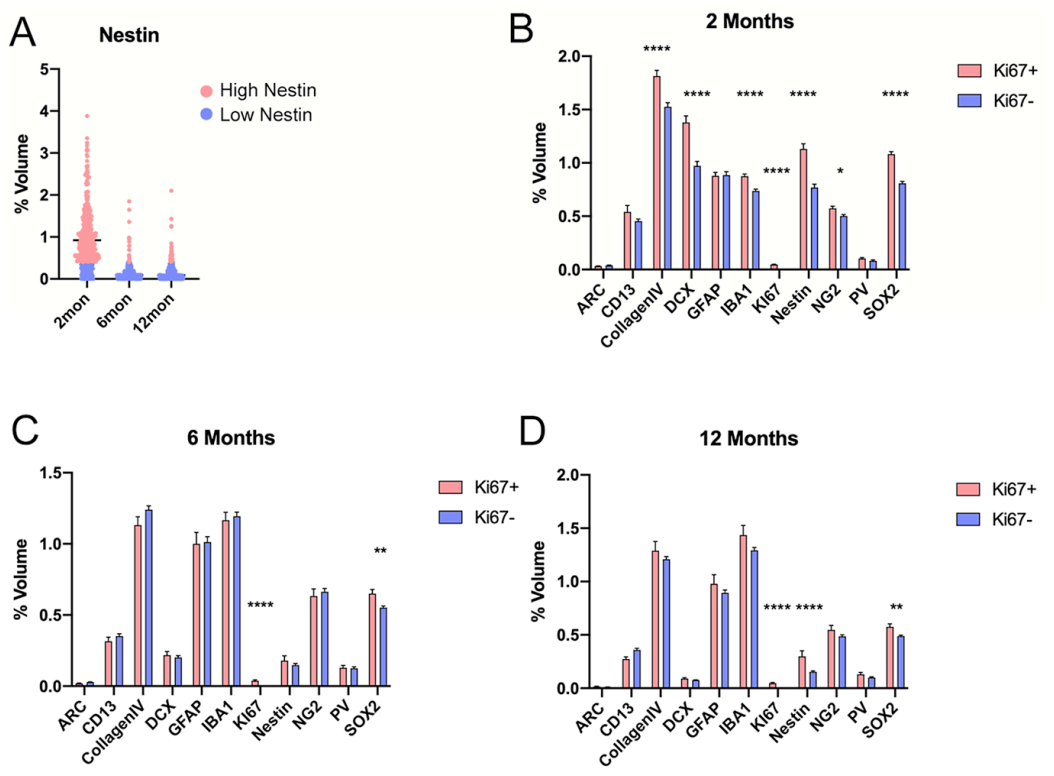

Figure 6 - Supplemental 1

(A) The volume of nestin-labeled radial processes within the random sampled spots. Spots in red were classified as high nestin populated while black represents low nestin spots. **(B-D)** Comparison of cell volumes in spots containing and lacking Ki67+ cells in the 2 month **(B)** For details of statistics please refer to Supplemental Table 1. * $p < 0.05$, ** $p < 0.01$, *** $p < 0.001$, **** $p < 0.0001$

Supplemental tables

Supplemental table 1: Values and statistics for graphs shown in main figures 1, 3, 4, 5, 6, 7 and supplemental 1 of figure 6.

Supplemental table 2: List of primary and secondary antibodies

Antibody	Species	Manufacturer	Dilution	RRID
ARC	Guinea pig	Synaptic Systems	1:500	AB_2619853
BLBP	Rabbit	Abcam	1:200	AB_880078
CD13	Goat	Novus	1:500	AB_2227288
Cleaved Caspase 3	Rabbit	Cell Signaling	1:150	AB_2341188
CollagenIV	Rabbit	Bio-Rad	1:750	AB_2082660
CTIP2	Rat	Abcam	1:250	AB_2064130
DOUBLECORTIN	Goat	Santa Cruz	1:300	AB_2088491
GFAP	Chicken	Novus	1:750	AB_1556315
Histone H3 Phospho S10	Mouse	Abcam	1:250	AB_443110
HOPX	Mouse	Santa Cruz	1:500	AB_2687966
IBA1	Rabbit	WAKO	1:500	AB_839504
ID4	Rabbit	Biocheck	1:250	AB_2814978
KI67	Rat	Bioscience	1:250	AB_10854564
LaminB1	Rabbit	Abcam	1:500	AB_10107828
MT3	Rabbit	Abcam	1:300	AB_2297959
Nestin	Mouse	BD	1:250	AB_396354
NeuroD1	Goat	Santa Cruz	1:250	AB_630922
NG2	Rabbit	Millipore	1:500	AB_11213678
OLIG2	Rabbit	Millipore	1:500	AB_570666
Parvalbumin	Mouse	Sigma	1:250	AB_477329
S100β	Rabbit	Abcam	1:500	AB_882426

SOX2	Rat	Invitrogen	1:250	AB_11219471
α-Chicken 488	Donkey	Jackson Laboratory	1:250	AB_2340375
α-Chicken 647	Donkey	Jackson Laboratory	1:250	AB_2340379
α-Goat 488	Donkey	Jackson Laboratory	1:250	AB_2336933
α-Goat 647	Donkey	Jackson Laboratory	1:250	AB_2340437
α-Goat Cy3	Donkey	Jackson Laboratory	1:250	AB_2307351
α-Guinea pig 488	Donkey	Jackson Laboratory	1:250	AB_2340472
α-Guinea pig 647	Donkey	Jackson Laboratory	1:250	AB_2340476
α-Mouse 488	Donkey	Jackson Laboratory	1:250	AB_2341099
α-Mouse 647	Donkey	Jackson Laboratory	1:250	AB_2340863
α-Mouse Cy3	Donkey	Jackson Laboratory	1:250	AB_2315777
α-Rabbit 488	Donkey	Jackson Laboratory	1:250	AB_2313584
α-Rabbit 647	Donkey	Jackson Laboratory	1:250	AB_2492288
α-Rabbit Cy3	Donkey	Jackson Laboratory	1:250	AB_2307443
α-Rat 488	Donkey	Jackson Laboratory	1:250	AB_2340684
α-Rat 647	Donkey	Jackson Laboratory	1:250	AB_2340694
α-Rat Cy3	Donkey	Jackson Laboratory	1:250	AB_2340667